The International Journal of Advanced Manufacturing Technology (2020) 108:2149–2164
https://doi.org/10.1007/s00170-020-05516-2

ORIGINAL ARTICLE

Optimization of hot backward extrusion process parameters for flat bottom cylindrical parts of Mg-8Gd-3Y alloy based on 3D processing maps

Jian Zeng[1] · Fenghua Wang[1] · Shuai Dong[1] · Li Jin[1] · Yu Fan[2] · Jie Dong[1]

Received: 22 February 2020 / Accepted: 19 May 2020 / Published online: 5 June 2020

Abstract
Based on three-dimensional processing maps and numerical simulation, a demo flat bottom cylindrical part (with outer diameter of 235 mm, wall thickness of 34 mm, and height of 255 mm) of high strength Mg-Gd-Y magnesium alloy was hot backward extruded by adding an outer flange to increase the overall deformation amount and strain uniformity. Firstly, on the basis of dynamic material model and Murty instability criterion, isothermal compression stress-strain curves of cast-homogenized Mg-8Gd-3Y alloy were used to construct the processing maps. The processing maps show that the formable domain is relatively narrow: at lower strain rates ranging from 0.001 to 0.006 s^{-1}, and the suitable temperature is from 350 to 450 °C; and at higher strain rates ranging from 0.006 to 0.1 s^{-1}, and the temperature is from 410 to 450 °C. Then, the processing maps were integrated into a finite element software to simulate the forming process of cylindrical parts, and the influences of deformation temperature and velocity on the power dissipation efficiencies of different positions of flanged cylindrical parts were mainly discussed. The simulation results indicate that the average strain of flanged cylindrical parts reaches 30.07% and is larger than that of unflanged cylindrical parts, and the standard deviation of the strain of flanged cylindrical parts is 19.35% and less than that of unflanged cylindrical parts. The optimal process parameters corresponding to the maximum power dissipation efficiency are the temperature of 430 °C and velocity of 1 mm/s. Finally, under the optimal forming condition, the hot backward extrusion experiments of flanged cylindrical parts were conducted. The experimental results exhibit that the flanged cylindrical parts could be properly formed with good surface quality, and have relatively uniform microstructures and mechanical properties. The difference of tensile strength between the bottom and cylindrical body is less than 5 MPa, and the hardness difference is less than 1.6 HV.

Keywords Magnesium alloy · Three-dimensional (3D) processing maps · Formability · Parameter optimization · Finite element (FE) simulation

1 Introduction

Compared with commercial magnesium (Mg) alloys, the newly developed Mg-Gd-Y alloys have remarkable age-hardening effect and much better mechanical properties [1–3]. The combination of light material and suitable configuration is of great importance to get maximum weight reduction for various parts or components [4, 5]. Therefore, light-weight flat bottom

✉ Shuai Dong
sjtuds@sjtu.edu.cn

Jian Zeng
jianzeng@sjtu.edu.cn

Fenghua Wang
wangfenghua@sjtu.edu.cn

Li Jin
J_jinli@sjtu.edu.cn

Yu Fan
yufan@hfut.edu.cn

Jie Dong
jiedong@sjtu.edu.cn

[1] National Engineering Research Center of Light Alloy Net Forming and State Key Laboratory of Metal Matrix Composite, School of Materials Science and Engineering, Shanghai Jiao Tong University, Shanghai 200240, China

[2] Anhui Province Key Lab of Aerospace Structural Parts Forming Technology and Equipment, Hefei University of Technology, Hefei 230009, China

cylindrical parts of Mg-Gd-Y alloys may be widely used in aviation, aerospace, and high-speed vehicle fields.

However, the formability of Mg alloys, especially high strength Mg rare-earth alloys, is very poor. The forming temperature range is narrow, and cracking is easy to occur during the hot forming process [6, 7]. The hot processing maps are one of the most effective methods to determine and optimize the process parameters and reflect the change of the hot formability of material with temperature, strain rate, and strain [8, 9]. So far, many efforts have been made in the processing maps of aluminum alloy [10, 11], titanium alloy [12, 13], and commercial Mg alloy [14–16]. Additionally, in the research on the processing maps of Mg rare-earth alloys, Xu et al. [17] constructed the hot processing maps of Mg-9Gd-2.9Y-1.9Zn-0.4Zr-0.2Ca alloy and determined the optimum hot working parameters at strain of 0.9. By comparison between the processing maps of as-cast Mg-7Gd-5Y-0.6Zn-0.8Zr alloy with those of solution treated alloy, it can be found that the solution treatment narrows the flow instability region of materials at low temperature and high strain rate and weakens the workability at high temperature [18]. However, the temperature, strain, and strain rate of large parts at different positions are not exactly the same and constantly changing during thermal forming process. Therefore, it is difficult to predict the formability of real parts accurately only through hot processing maps. Recently, the combination of FE simulation technology and 3D processing maps, which can effectively predict the formability of materials in different locations of workpiece and at different moments of forming process, has become an important means to investigate the workability of the material and identify the appropriate processing window during hot deformation [3, 8, 14].

The flat bottom cylindrical parts are usually made by hot backward extrusion, but the nonuniform strain occurs easily during the extrusion process [19, 20]. For example, due to the friction at the bottom of concave die, the bottom of the cylindrical parts will inevitably exhibit a hard deformation zone (usually called “dead zone”) [21, 22]. Since the top material of cylindrical parts only undergoes rigid translation along the opposite direction of extrusion during the later forming process, no plastic deformation happens, and the cumulative deformation of the top material is small after backward extrusion [21]. Mg alloy is the hexagonal close-packed crystal structure and has poor deformation coordination at room temperature. The fine and uniform recrystallization structure is crucial for improving the mechanical property of materials, especially plasticity [7]. The recrystallization behavior of high strength Mg-Gd-Y alloy is sensitive to process parameters such as temperature and strain, and the material is easier to obtain small microstructure under the conditions of lower temperature and larger strain [6]. Therefore, the backward extrusion process needs to be optimized to improve the overall deformation and strain uniformity of the material.

Therefore, in this paper, an outer flange was introduced at the top of a demo flat bottom cylindrical part to study and improve the overall deformation amount and strain uniformity. With the aid of the integration of 3D processing maps and FE calculation, the optimal extrusion parameters were obtained. Real vertical backward extrusion experiments were performed to check the effects of outer flange on the uniformity of the microstructures and mechanical properties.

2 Materials and methods

The semi-continuous cast rod of Mg-8Gd-3Y (GW83) alloy with a diameter of 180 mm after homogenization was selected as the experimental material in the present work, and its chemical composition is Mg-8Gd-3Y-0.5Zr (in wt.%). The initial optical microstructure after homogenization is presented in Fig. 1. It can be seen that the material exhibits the equiaxed microstructure with an average grain size of about 136 μm. To ensure the uniformity of the performance for all samples, the cylindrical specimens were cut from the cast-homogenized rod along the length direction. In this paper, the size of sample for compression is the same as that in our former paper [23], and the tested machine and method are also identical. However, the tested parameters are different. The temperature was 300 °C, 350 °C, 400 °C, and 450 °C. The strain rate was 0.001 s^{-1}, 0.01 s^{-1}, 0.1 s^{-1}, and 1 s^{-1}, and the strain was 1.0.

The sketch map of flat bottom cylindrical parts, as shown in the black solid lines of Fig. 2, has an outer diameter of 235 mm, a wall thickness of 34 mm, and a height of 255 mm. To make the end metal flow severely at the later stage of forming and increase the amount of deformation, an outer flange with outer diameter of 310 mm and thickness of 15 mm was designed at the end of the flat bottom cylindrical parts, as shown in the red dotted line of Fig. 2.

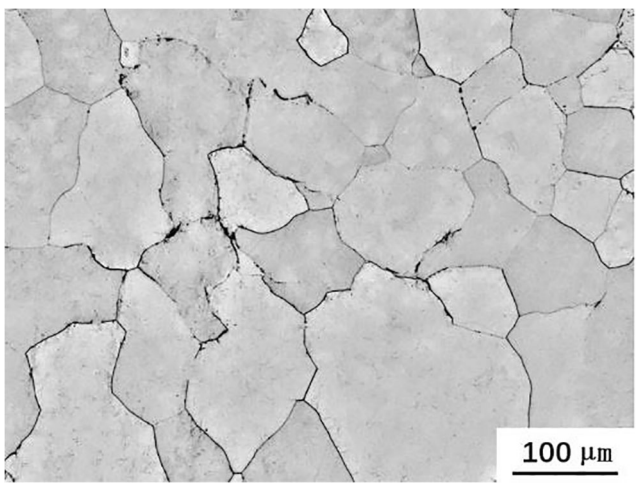

Fig. 1 Initial microstructure of cast-homogenized GW83 alloy

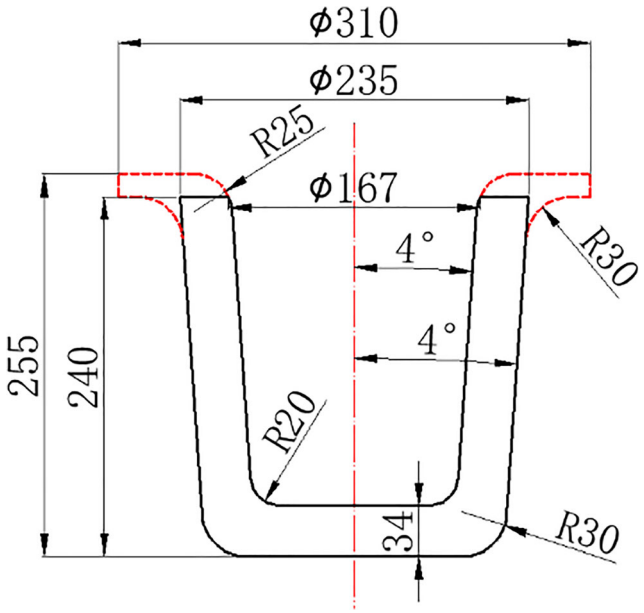

Fig. 2 The sketch map of flat bottom cylindrical parts and flanged cylindrical parts

By means of the secondary development, the 3D processing maps were coupled into the FE software Deform-3D to analyze the formability of the backward extrusion of cylindrical parts. The FE models for the backward extrusion of flat bottom cylindrical parts and flanged cylindrical parts are shown in Fig. 3a and b, respectively. Due to the symmetry of the model about the vertical mid-plane, one in eight samples was used for simulation to reduce the simulation time. The simulated temperatures of billet, dies, and ambient air were all set to the same value. The friction coefficients between workpiece and dies are 0.20. The heat transfer coefficient between workpiece and air is 20 N/(s m °C), and the heat transfer coefficient between billet and dies is 11,000 N/(s m °C). The billet was divided by the absolute grid method, and the tetrahedral mesh was selected for mesh type. The minimum and maximum mesh sizes were set to 0.25 mm and 0.50 mm, respectively. The diameters of the billets of flat bottom cylindrical parts and flanged cylindrical parts are all 170 mm, and the heights of the billets of flat bottom cylindrical parts and flanged cylindrical parts are 240 mm and 272 mm, respectively.

The isothermal backward extrusion experiments were performed on a 6000 tons hydraulic press under the optimum process parameters. The die structure of backward extrusion is represented in Fig. 4. By adding a flash gutter at the flange, the excess metal can be accommodated. Firstly, the molds were heated to the forming temperature and held isothermally for 12 h, and the billets were heated to the deformation temperature and kept for 4 h to ensure the uniform temperatures of the molds and billet. Then, the moveable table of the press was used to quickly install the dies, and the lubricant was sprayed on the surfaces of dies. Finally, the billet was put into the dies for backward extrusion. After extrusion, the cylindrical parts

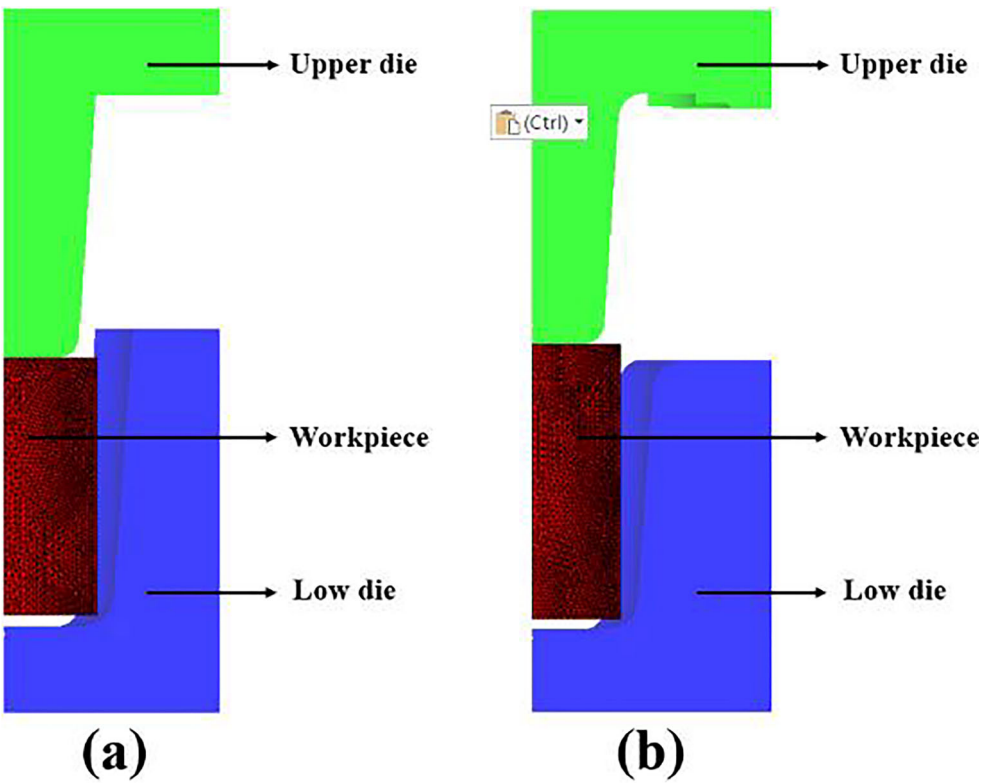

Fig. 3 The FE models for the backward extrusion of **a** flat bottom cylindrical parts and **b** flanged cylindrical parts

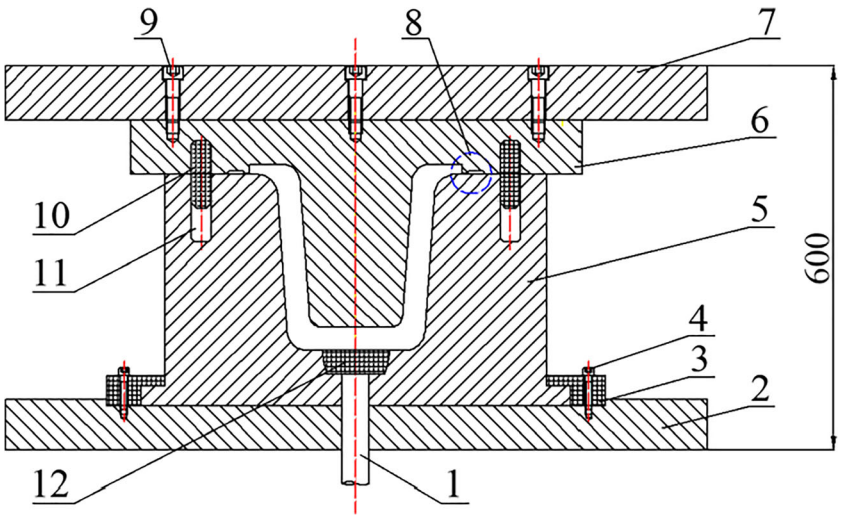

Fig. 4 Schematic of the die structure of flanged cylindrical parts backward extrusion. (1) Ejector beam. (2) Lower platen. (3) Lower briquetting. (4) Bolt of lower briquetting. (5) Female die. (6) Male die. (7) Upper platen. (8) Flash gutter. (9) Connecting bolt. (10) Guide pin. (11) Guide hole. (12) Ejector tray

were quenched rapidly to preserve the deformed microstructure.

The deformed workpiece was cut along the axial direction, and four positions of cylindrical parts were taken for microstructure observation. The cut sample was mounted, polished, and etched. The machine for microstructure observation and the etchant are consistent with those in our former paper [3]. To analyze the mechanical properties of the flat bottom cylindrical parts after extrusion, the tensile test bars were machined at four positions of cylindrical parts. The tensile tests were carried out on the Instron 5982 test machine, and the tensile speed is 1 mm/min.

3 Results and discussion

3.1 True stress-strain curves

Based on the isothermal compression data, the change of flow stress with strain of cast-homogenized GW83 alloy under various compression conditions is displayed in Fig. 5. From Fig. 5, the temperature and strain rate have a remarkable effect on the flow stress, and the stress increases obviously as the temperature decreases or the strain rate increases. At first, the stress rises rapidly. This is mainly related to the two kinds of microstructural changes of the material. On the one hand, the dislocation multiplication and entanglement make the material work harden. On the other hand, the dislocation merger and recombination occur under the action of thermal activation and external force, which results in dynamic recovery and softening of material. The two mechanisms proceed at the same time and compete with each other, but the effect of work hardening is obviously stronger than that of dynamic softening in the initial stage [7], which makes the stress increase continuously. After the peak stress, the softening caused by dynamic recrystallization overtakes work hardening [7], and the curves begin to decrease.

3.2 3D processing maps

The 3D processing maps, which are composed of the 3D power dissipation map and 3D flow instability map, describe the distribution of the power dissipation efficiency and flow instability regions under the various deformation conditions [8]. The power dissipation efficiency and the size of flow instability region are changing with strain rate, temperature, and strain [3, 8].

3.2.1 3D power dissipation map

It is assumed that the flow stress at a given forming temperature and strain conforms to the dynamic material model (DMM), which regards the hot plastic deformation of a workpiece as a dissipator of power and is expressed as [9, 24]:

$$\sigma = K\dot{\varepsilon}^m \tag{1}$$

where K is a material constant and m represents the strain rate sensitivity index which is shown below:

$$m = \frac{\partial \ln\sigma}{\partial \ln\dot{\varepsilon}} \tag{2}$$

Under any given condition, the total dissipation power P, which was absorbed by the workpiece during the plastic deformation, mainly consists of G content and J co-content:

$$P = \sigma \cdot \dot{\varepsilon} = G + J = \int_0^{\dot{\varepsilon}} \sigma d\dot{\varepsilon} + \int_0^{\sigma} \dot{\varepsilon} d\sigma \tag{3}$$

where G is the power dissipated by plastic deformation, and the power is mainly converted into the viscoplastic

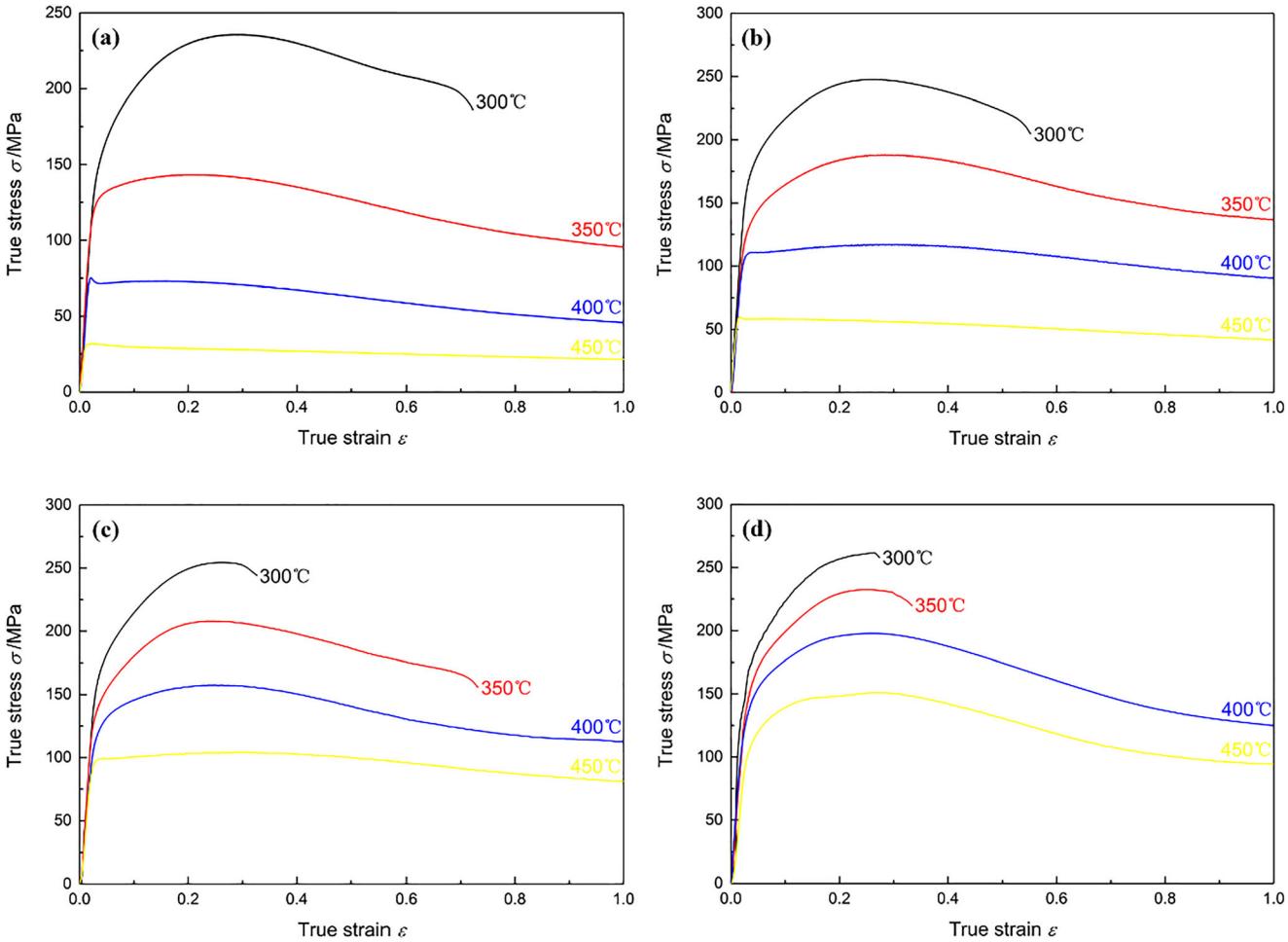

Fig. 5 True stress-strain curves of cast GW83 alloy at different strain rates. **a** $\dot{\varepsilon} = 0.001\ s^{-1}$. **b** $\dot{\varepsilon} = 0.01\ s^{-1}$. **c** $\dot{\varepsilon} = 0.1\ s^{-1}$. **d** $\dot{\varepsilon} = 1\ s^{-1}$

heat; J is the power dissipation of metallurgical processes such as dynamic recovery, dynamic recrystallization, and super plastic flow. The ratio of G to J during thermal deformation is determined by the constitutive flow behavior of the material and defined as strain rate sensitivity index (m).

$$\frac{dJ}{dG} = \frac{\dot{\varepsilon}}{\sigma}\frac{d\sigma}{d\dot{\varepsilon}} = \frac{d\ln\sigma}{d\ln\dot{\varepsilon}} = m \tag{4}$$

In comparison of the J with its maximum values J_{max}, the power dissipation efficiency η is defined and written as:

$$\eta = \frac{J}{J_{max}} = \frac{2m}{m+1} \tag{5}$$

where J_{max} is referred to a linear dissipator ($m = 1$).

The power dissipation efficiency not only describes the internal entropy production of the material during hot working but also represents the ability to dissipate energy through microstructure evolution. Different microscopic mechanisms correspond to different values of η [25], so the size of η reflects the microscopic response of materials at varying deformation parameters. These microscopic mechanisms include safety mechanisms such as dynamic recrystallization, dynamic recovery, and superplasticity. They also contain non-safety mechanisms including ductile fracture, wedge fracture, intergranular fracture, and flow instability mechanisms such as flow localization and adiabatic shear deformation.

On the basis of the above-mentioned tested curves, the values of flow stress under various strains can be determined at a certain temperature and strain rate, then the values of η can be calculated. After that, the temperature, strain rate, and strain were taken as the three-dimensional coordinate axis. By plotting color grid map of the parameter η, as shown in Fig. 6, the 3D power dissipation map was constructed. The grid color of each point in Fig. 6 represents the value of power dissipation efficiency.

The higher the power dissipation efficiency, the greater the proportion of the energy input to the microstructure evolution, such areas are most favorable to plastic deformation, and the formability is better [13]. From Fig. 6, GW83 alloy exhibits

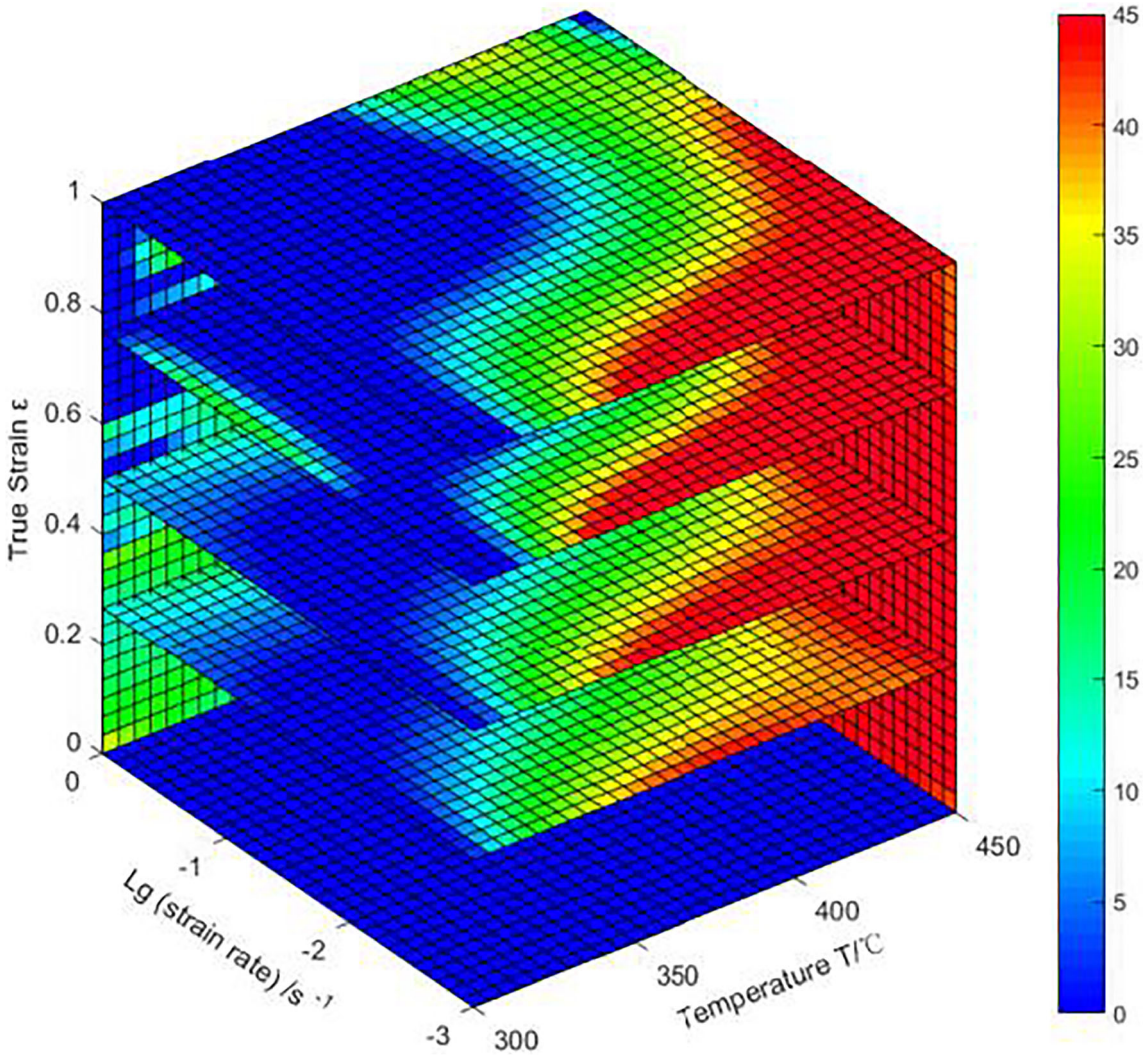

Fig. 6 The 3D power dissipation map

two peak power dissipation regions: 350–450 °C at 0.001–0.006 s^{-1} with the average peak efficiency of about 34%, and 410–450 °C at 0.006–0.1 s^{-1} with the average peak efficiency of about 38%.

3.2.2 3D flow instability map

Besides the power dissipation map, a 3D flow instability map is essential for the more comprehensive analysis of formability [3]. Choosing an appropriate flow instability criterion is the primary task for constructing the 3D flow instability map. At present, there are six main criteria of flow instability [26], including Murty criterion, Semiatin criterion, Jonas criterion, Gegel criterion, Prasad criterion, and Alexander criterion. It has been proved that the Murty criterion is one of the most commonly used and applicable to any type of flow curves [27, 28]. Therefore, Murty instability criterion was selected to establish the 3D flow instability map of GW83 alloy, which can be expressed as:

$$2m-\eta < 0 \tag{6}$$

The 3D flow instability map is presented in Fig. 7, where the blue areas are the regions of flow stability and the red areas are the regions of flow instability. From Fig. 7, the temperature, strain, and strain rate have an influence on the variation of flow instability regions. Additionally, the flow instability regions gradually increase with increasing strain. When the strain increases to 1.0, the instability regions concentrate in two areas: in the temperature range of 300–320 °C and strain rate range of 0.001–1 s^{-1}, in the temperature range of 320–380 °C and strain rate range of 0.02–1 s^{-1}.

In summary, the optimum forging process parameters of cast GW83 alloy were determined at 350–450 °C and 0.001–0.006 s^{-1}, and 410–450 °C and 0.006–0.1 s^{-1}.

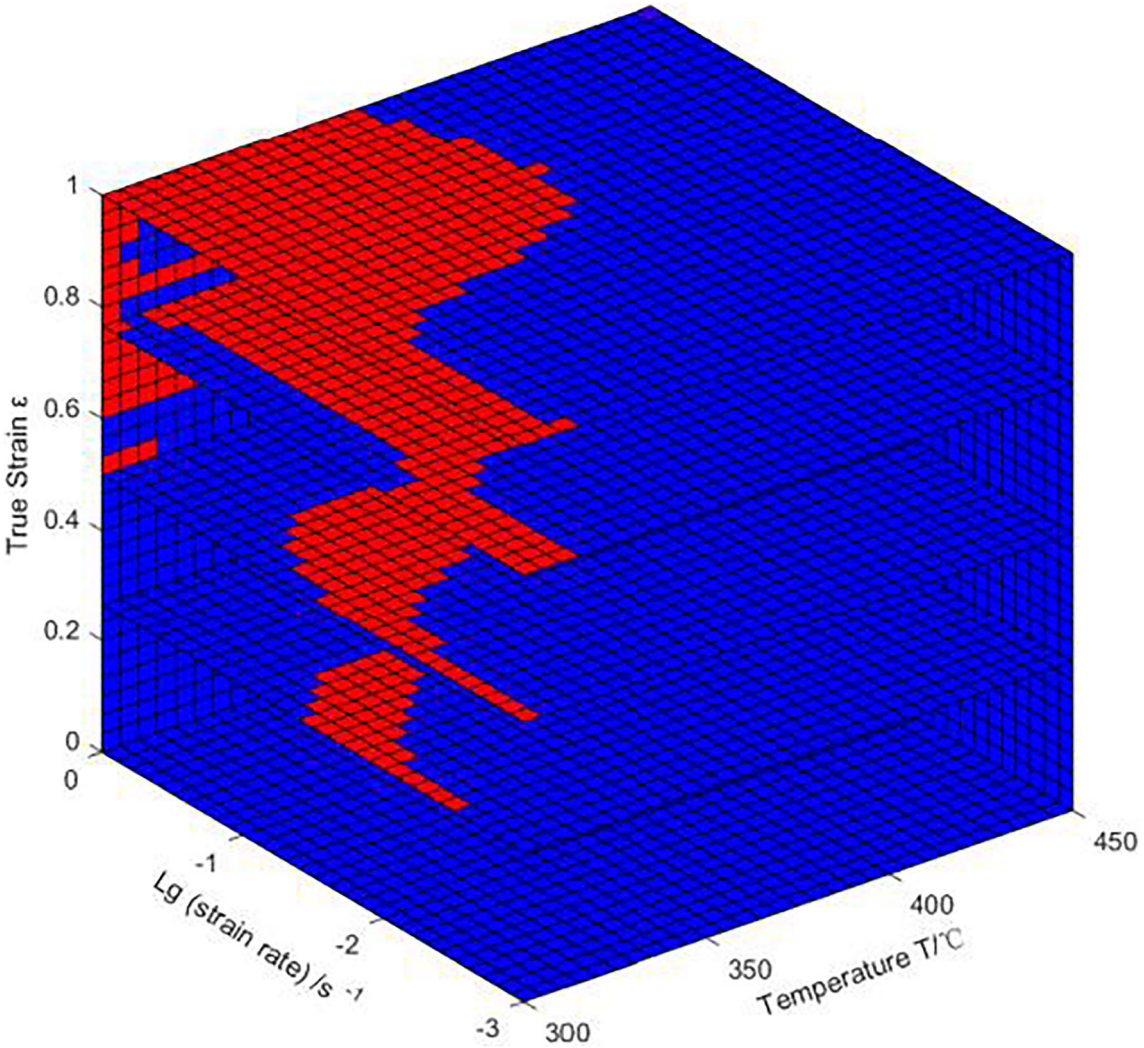

Fig. 7 The 3D flow instability map

4 FE simulation of backward extrusion of cylindrical parts

4.1 Effect of the flange on the effective strain amount and uniformity

Figure 8 shows the distributions of the effective strain rate during the backward extrusion process of flat bottom cylindrical parts. From Fig. 8, the strain rates of different parts of the sample vary greatly during the whole deformation process, which is mainly due to the existence of friction. In the early stage shown in Fig. 8a, the larger effective strain rate mainly focuses on the upper corner region at the bottom of the cylinder, and the other regions all have a small value. Then, the region with large effective strain rate expands gradually, as shown in Fig. 8b and c. After deformation, the maximum effective strain rate is concentrated on the bottom area and upper end of the cylinder.

Figure 9 is the effective strain distributions during the backward extrusion process of flat bottom cylindrical parts. It can be found that the effective strain of the end of cylindrical parts is small during the backward extrusion process, because the end metal is always in free flow state. Through calculation, the average effective strain of each node is 1.43 after simulation, and the standard deviation (SD) of the effective strains of these nodes is 0.93. In addition, it can be found that the effective strains of the bottom corner regions and most of end regions after deformation are lower than 0.75, which is far lower than the average effective strain. This will lead to the insufficient dynamic recrystallization of the end and bottom corner regions. Compared with other positions, the mechanical properties of the two positions are poor, and there is inconsistency in the performance of flat bottom cylindrical parts.

Figure 10 shows the distributions of the effective strain rate during the backward extrusion process of flanged

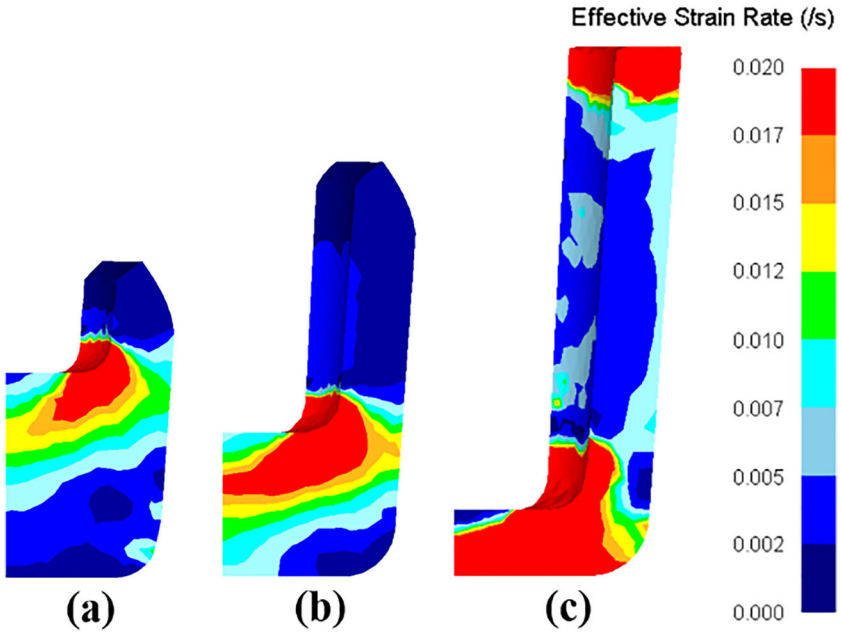

Fig. 8 Distributions of effective strain rate during the backward extrusion process of flat bottom cylindrical parts. **a** 120 mm. **b** 170 mm. **c** 220 mm

cylindrical parts. It can be seen that the effective strain rates of different areas of the sample are different. During the deformation process, the distributions of the effective strain rate in Fig. 10 are basically the same as those of Fig. 8. After deformation, the bottom area and the flange of flanged cylindrical parts have the maximum effective strain rate.

Figure 11 is the effective strain distributions during the backward extrusion process of flanged cylindrical parts. It can be observed that the effective strains in the end regions are higher than 0.75 after deformation. The average effective strain of each node can be calculated and is 1.86 after simulation. The overall deformation of material is greatly improved and increased by about 30.07% compared with the value of Fig. 9. This makes each position of the flat bottom cylindrical parts undergo more recrystallization and improves the overall performance during the deformation process. After simulation, the SD of effective strain is 0.75 and decreases by 19.35% in comparison with that of Fig. 9, indicating that the property of materials may be more consistent.

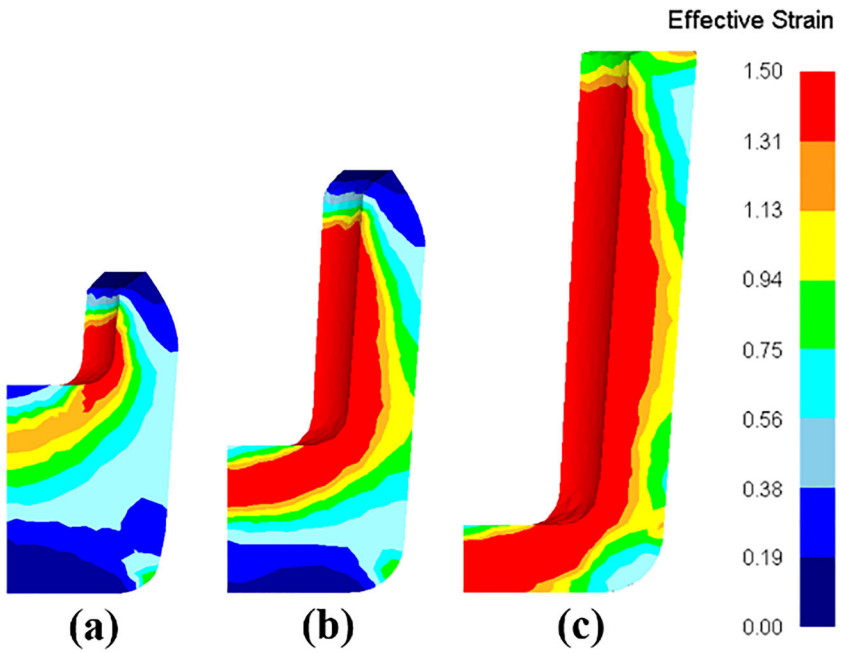

Fig. 9 Distributions of effective strain during the backward extrusion process of flat bottom cylindrical parts. **a** 120 mm. **b** 170 mm. **c** 220 mm

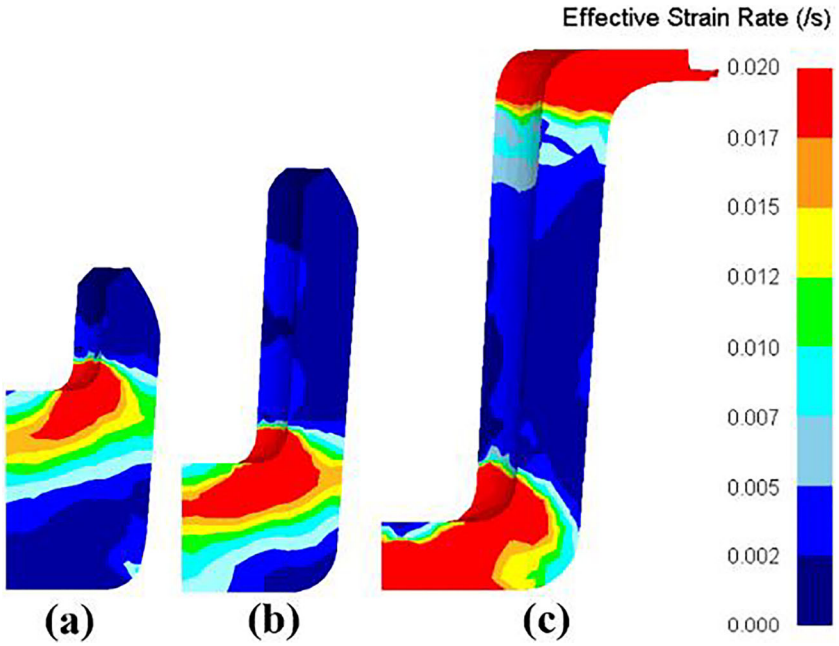

Fig. 10 Distributions of effective strain rate during the backward extrusion process of flanged cylindrical parts. **a** 142 mm. **b** 202 mm. **c** 252 mm

4.2 Effect of forming velocity on the formability of backward extrusion

To obtain the optimal extrusion parameters, the simulations of backward extrusion of flanged cylindrical parts at varying parameters were carried out by combining the 3D processing maps with FE simulation.

First of all, the different deformation velocities at a temperature of 430 °C, which are listed in Table 1, were selected to investigate the effect of velocity on the formability during the backward extrusion of flanged cylindrical parts. According to 3D processing maps, it can be found that 430 °C is the parameter of safety regions, which is outside the flow instability regions.

The power dissipation efficiency distributions after deformation under six groups of parameters are shown in Fig. 12. As can be seen from Fig. 12, the power dissipation efficiency of each position of cylindrical parts is greater than 0, indicating that no flow instability occurs during the backward extrusion process. It can be concluded that the stable deformation happened under the parameters of safety region, which suggests that the material has good formability.

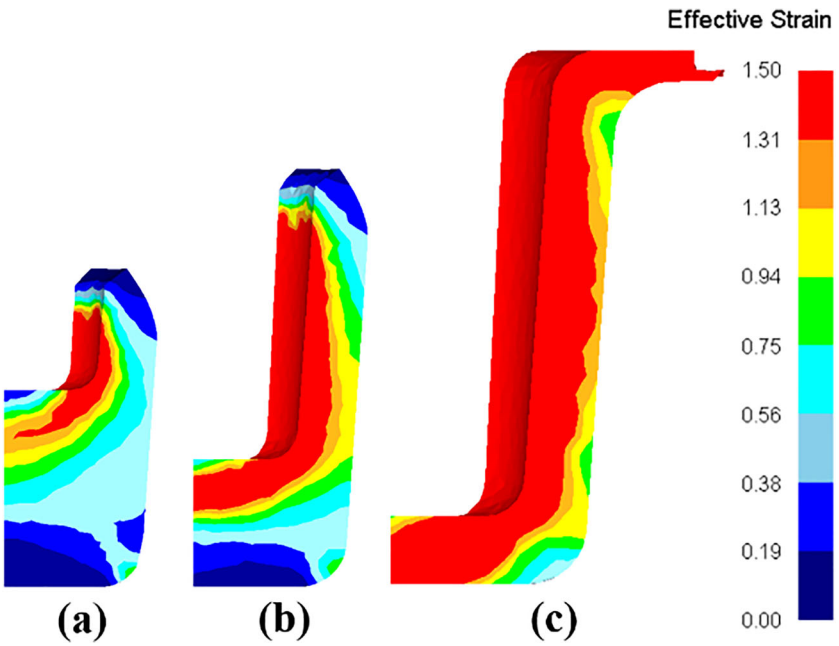

Fig. 11 Distributions of effective strain during the backward extrusion process of flanged cylindrical parts. **a** 142 mm. **b** 202 mm. **c** 252 mm

Table 1 The process parameters used for simulation under different velocities

Item	Temperature /°C	Velocity/mm/s	Strain/mm/mm
1	430	0.25	1
2	430	0.5	1
3	430	1	1
4	430	2	1
5	430	4	1
6	430	8	1

Subsequently, as shown in Fig. 13a, the four positions after deformation were selected to compare the power dissipation efficiency. Position A is located at the bottom of flanged cylindrical parts. Position B is located at the lower part of the cylindrical body. Position C is located at the upper part of the cylindrical body. Position D is located at the flange part. Figure 13b and c are the distributions of the power dissipation efficiency at different process parameters. It was obvious that the power dissipation efficiencies of different positions under different parameters are different. From Fig. 13b, as the forming velocity increases, the values of η of the material increase first and then decrease. The power dissipation efficiency of each position under the third set of parameters

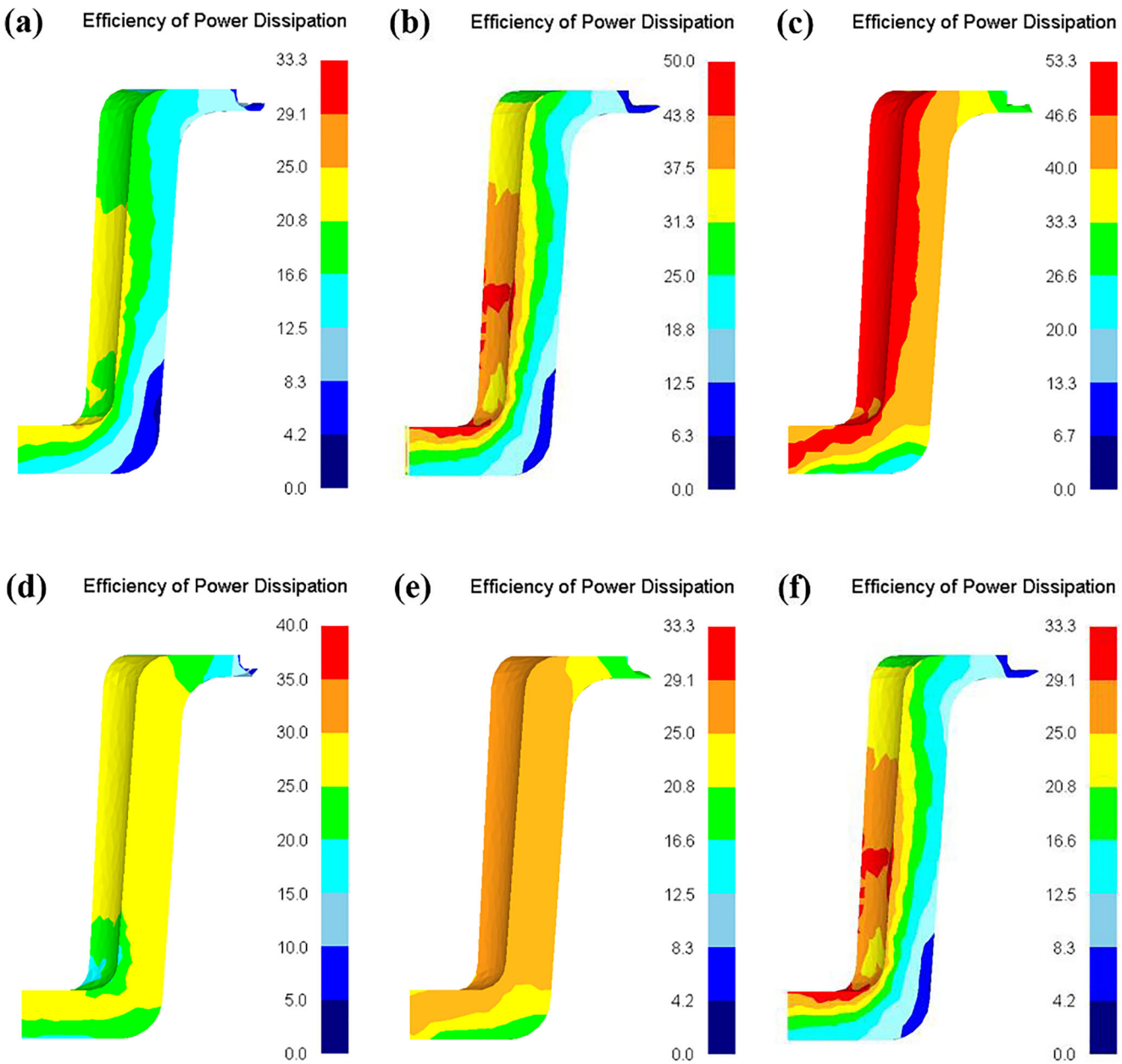

Fig. 12 Distributions of power dissipation efficiency under different velocities. **a** 0.25 mm/s. **b** 0.5 mm/s. **c** 1 mm/s. **d** 2 mm/s. **e** 4 mm/s. **f** 8 mm/s

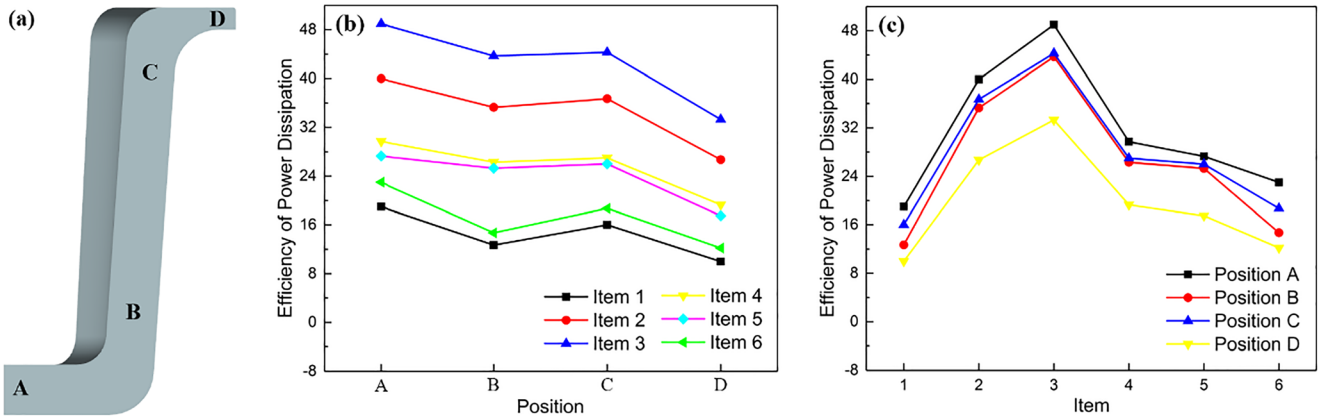

Fig. 13 **a** Four positions selected for the measurement of power dissipation efficiency and the power dissipation efficiencies. **b** At different positions. **c** At different items

reaches the maximum value, showing that the material possesses the best formability under this condition. Under the first set of parameters, the power dissipation efficiency of each position is the smallest, and the formability of the material is the worst. It can be found from Fig. 13(c) that the values of η at position A are the largest at varying parameters, and the formability is the best. The power dissipation efficiency at position D is the smallest and the formability is the worst, that is, the flange is not easy to form. Additionally, under most of the conditions, the power dissipation efficiencies at position B and position C are very close, and the formability of the two positions is roughly the same.

4.3 Effect of forming temperature on the formability of backward extrusion

As listed in Table 2, the influence of temperature on the formability was investigated. The simulation parameters are as follows: the forming velocity of 1 mm/s and the temperatures of 410 °C, 430 °C, and 450 °C. It can be seen from 3D flow instability map that these deformation parameters are outside the flow instability regions and belong to the safety regions.

After simulation, the power dissipation efficiency distributions under three groups of parameters are presented in Fig. 14. From Fig. 14, the power dissipation efficiency of each position is greater than 0, and no flow instability occurs.

Table 2 The process parameters used for simulation under different temperatures

Item	Temperature/°C	Velocity/mm/s	Strain/mm/mm
1	410	1	1
2	430	1	1
3	450	1	1

As shown in Fig. 13a, four same positions were selected to measure the power dissipation efficiency after simulation. Figure 15a and b are the distributions of the power dissipation efficiencies under various conditions. It can be found that the power dissipation efficiencies at different parameters and positions are various. Figure 15a shows that as the temperature increases, the power dissipation efficiency increases and then decreases, and the value of power dissipation efficiency is maximum under the second set of parameters. Under the first set of low temperature parameters, the power dissipation efficiency of each position is smallest, and the formability is the worst. Figure 15b shows that the power dissipation efficiencies at position A and position D are also the largest and smallest values under different parameters, respectively, suggesting that the flange is the most difficult position to form at different temperatures. In addition, it can be seen that the power dissipation efficiencies at positions B and C are also similar, and the formability is basically the same.

In conclusion, the best forming parameters of backward extrusion of flanged cylindrical parts are the deformation temperature of 430 °C and velocity of 1 mm/s.

5 Backward extrusion experiments, microstructures, and mechanical properties of flanged cylindrical parts

5.1 Backward extrusion experiments

To validate the reliability of the simulation results, the isothermal experiments of backward extrusion of flanged cylindrical parts were performed under the deformation condition of 430 °C and 1 mm/s. The extrusion dies are presented in Fig. 16a, and the flanged cylindrical part after experiment is shown in Fig. 16b. It was obvious that there is no crack on the surfaces of the sample, which shows that the material has good formability under this forming condition.

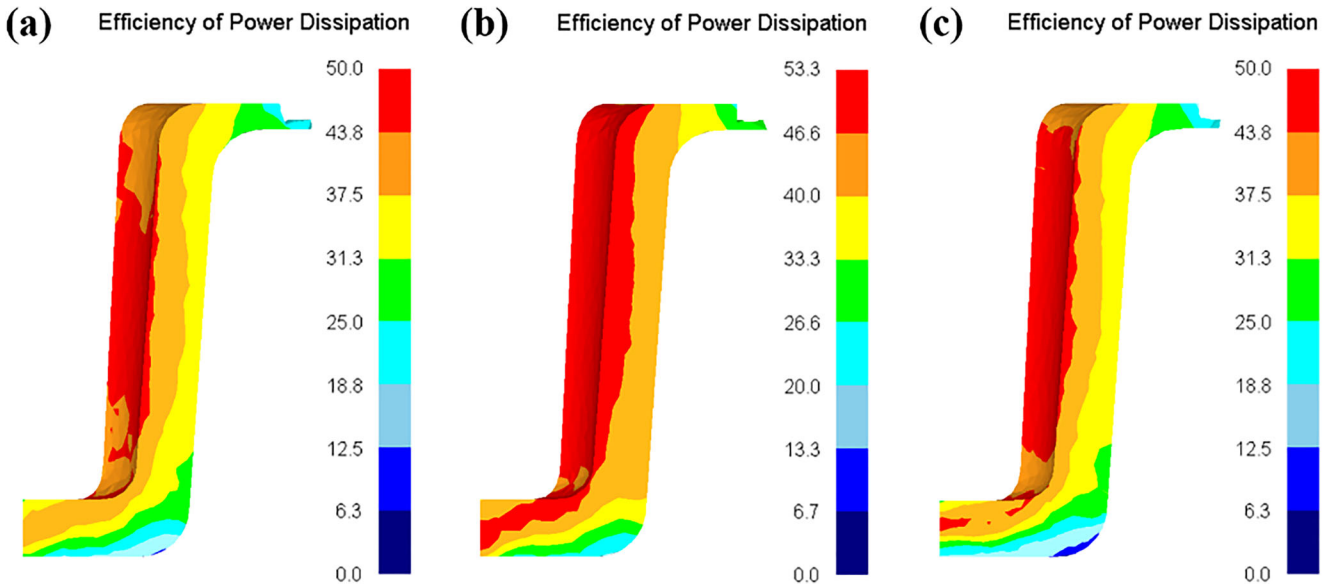

Fig. 14 Distributions of power dissipation efficiency under different temperatures. **a** 410 °C. **b** 430 °C. **c** 450 °C

5.2 Microstructures

Then, using the same four positions shown in Fig. 13a, the microstructures were observed after deformation, which are presented in Fig. 17a–d. In Fig. 17a, the material was almost completely recrystallized, and only a few deformed grains were compressed and elongated along the direction perpendicular to the extrusion. The recrystallization degree of position A is the highest. It can be seen from Fig. 17b and c that dynamic recrystallization is also relatively sufficient, and a few deformed grains were compressed and elongated along the extrusion direction. The dynamic recrystallization degree at the two positions has little difference and is slightly lower than that at position A. As shown in Fig. 17d, the dynamic recrystallization occurred only at the original grain boundary, and the microstructure was composed of the original deformed grains and small dynamic recrystallization grains. This is because the dislocations are hindered by the original grain boundaries, and the local dislocations build up faster during the forming process, which provides the critical dislocation density for the initiation of recrystallized grain [29]. The degree of recrystallization at this position is the smallest, which may be due to the final formation of the flange position and the decrease of billet temperature during the forming process of the flange. Dynamic recrystallization is a safe deformation, and the material has good formability under this condition. The material has the

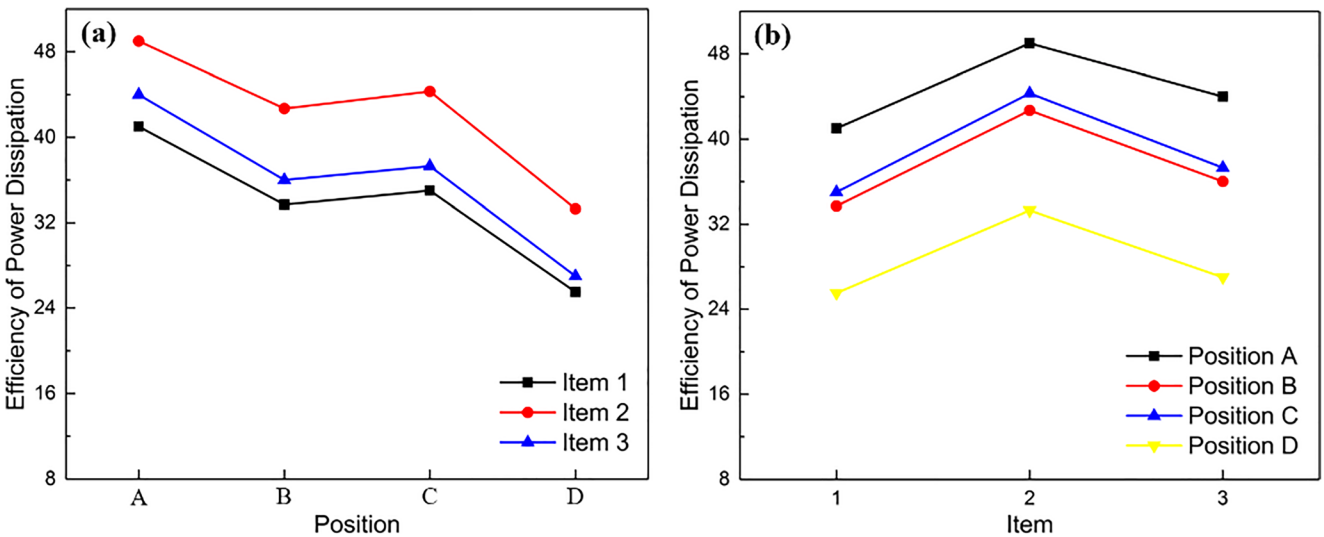

Fig. 15 The power dissipation efficiencies. **a** At different positions. **b** At different items

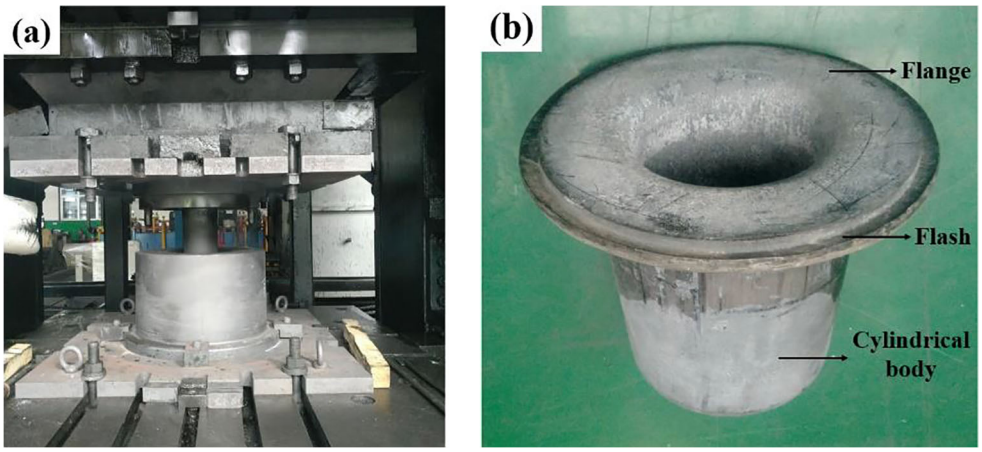

Fig. 16 **a** The experimental dies and **b** the flanged cylindrical parts after backward extrusion

highest degree of dynamic recrystallization at position A, followed by positions B and C, and the lowest degree is at position D. This is basically consistent with the order of the power dissipation efficiencies of the four positions after simulation. This indicates that the larger the η, the greater the dynamic recrystallization degree, and the better the formability of material. It also further verifies the reliability of the simulation results.

5.3 Mechanical properties

As shown in Fig. 13, the tensile specimens were taken at the position A and position D along the direction perpendicular to the extrusion, which were taken at the positions B and C along the extrusion direction. The tensile mechanical properties of the four positions are shown in Fig. 18. It was obvious that the material at position A has the best performance. The yield

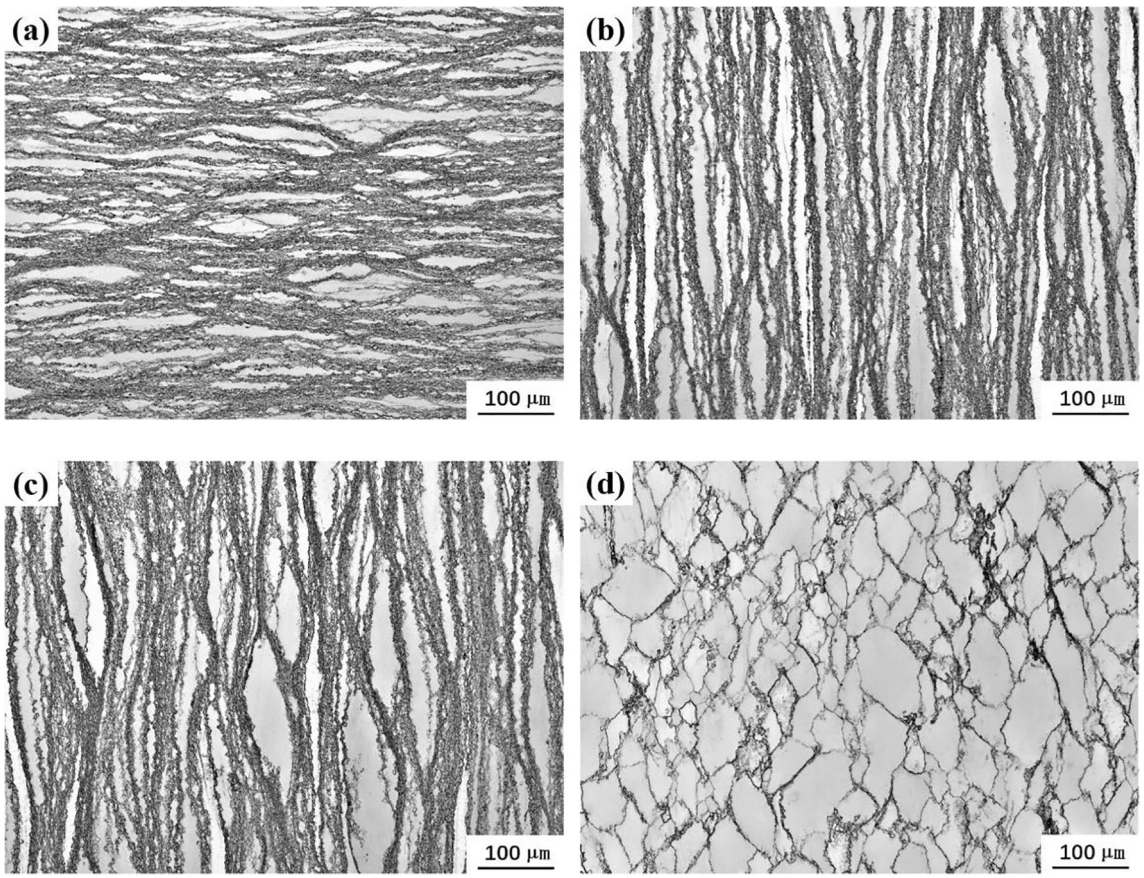

Fig. 17 The microstructures after backward extrusion of flanged cylindrical parts at **a** position A, **b** position B, **c** position C, and **d** position D

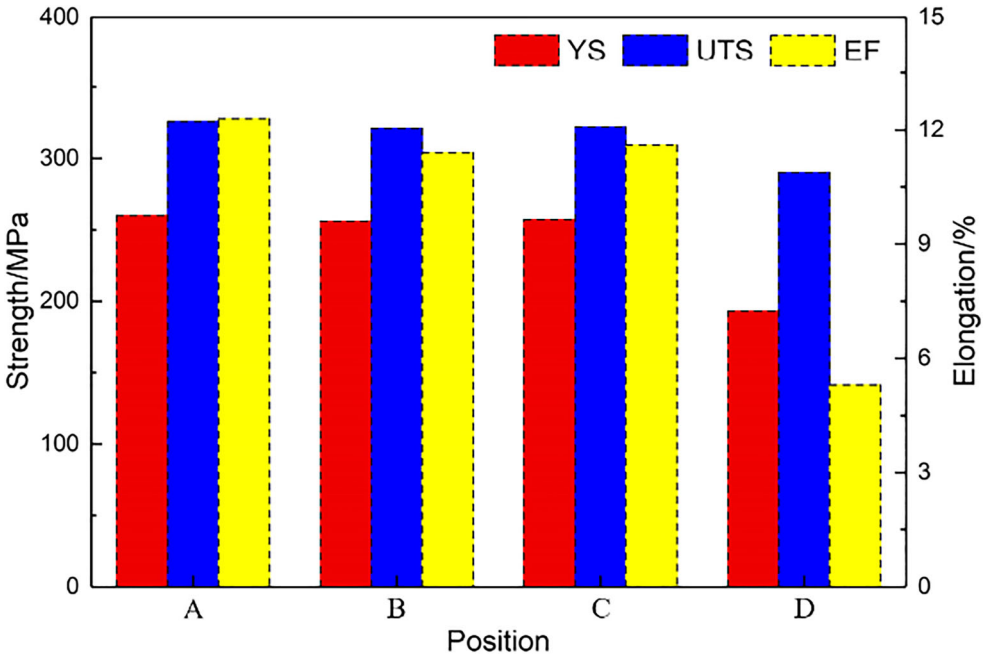

Fig. 18 The tensile mechanical properties of flanged cylindrical parts at different positions

strength (YS), ultimate tensile strength (UTS), and elongation to fracture (EF) are 262 MPa, 326 MPa, and 12.3%, respectively. The performances of positions B and C are basically the same and not significantly different from that of position A. The performance difference between the bottom and cylindrical body is less than 5 MPa, which means that the performance of the flat bottom cylindrical parts is relatively stable. The performance at position D is the worst. The YS, UTS, and EF of flange are 193 MPa, 290 MPa, and 5.3%, respectively, which are lower than the first three positions. The decrease of YS at position D can be attributed to the large grain size. Additionally, due to the fewer grains in the flange position, the stress cannot be dispersed to more grains during the tensile process, and the stress concentration is strong. The material is prone to crack, and the EF is low.

Figure 19 shows the hardness values at the four positions of the flanged cylindrical parts. It can be seen that the hardness at position D is the smallest, and the value is 73.6 HV. The

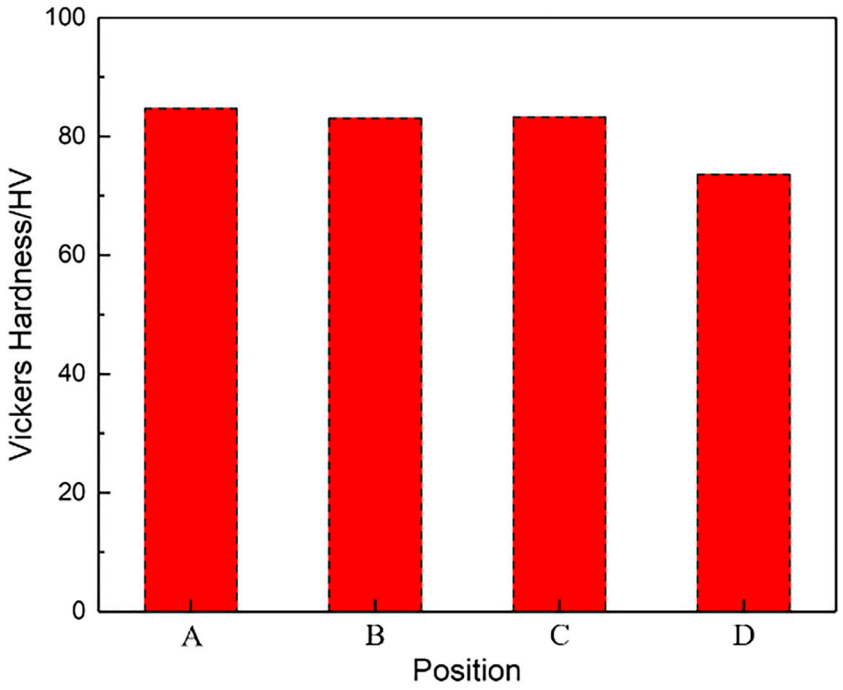

Fig. 19 The hardness values of flanged cylindrical parts at different positions

hardness values at positions A, B, and C are 84.7 HV, 83.1 HV, and 83.3 HV, respectively, which are much higher than that at position D. This is mostly due to the grain refinement caused by dynamic recrystallization. The hardness values of positions A, B, and C are roughly the same, and the hardness difference between the bottom and cylindrical body is lower than 1.6 HV, which shows that the performance of flat bottom cylindrical parts is relatively consistent.

6 Conclusions

1. The 3D processing maps were established. The preferred regions of the cast GW83 alloy for hot working were determined at 350–450 °C and 0.001–0.006 s^{-1}, and 410–450 °C and 0.006–0.1 s^{-1}.
2. The numerical simulation results show that, by adding an outer flange on the top of a demo flat bottom cylindrical part, the overall deformation and strain uniformity can be increased. The strain of flanged cylindrical parts is 30.07% larger than that of unflanged cylindrical parts, and the SD of strain of flanged cylindrical parts is 19.35% less than that of unflanged cylindrical parts.
3. Based on 3D processing maps, the numerical simulation results indicate that the formability of the demo flat bottom cylindrical part increases first and then decreases with increasing forming velocity or temperature, and the optimal temperature is 430 °C and velocity is 1 mm/s.
4. Under the optimal parameters, the demo flat bottom cylindrical parts were successfully extruded with good surface quality. The parts have relatively uniform microstructures and mechanical properties, and the difference of UTS between the bottom and cylindrical body is less than 5 MPa, and the hardness difference is less than 1.6 HV.

Funding information This work was financially supported by the National Key Research and Development Program of China (Grant No. 2016YFB0301103), the National Natural Science Foundation of China (Grant No. 51701117 and Grant No. 51601112), and the Fundamental Research Funds for the Central Universities of China (Grant No. PA2019GDPK0048).

References

1. Xie ZY, Tian Y, Li Q, Zhou JC, Meng Y (2019) Effects of forming parameters on microstructure and mechanical properties of a cup-shaped Mg–8.20Gd–4.48Y–3.34Zn–0.36Zr alloy sample manufactured by thixoforming. Int J Adv Manuf Technol 101: 1807–1819
2. Alizadeh R, Mahmudi R, Ruano OA, Ngan AHW (2017) Constitutive analysis and hot deformation behavior of fine-grained Mg-Gd-Y-Zr alloys. Metall Mater Trans A 48A:5699–5709
3. Zeng J, Wei XX, Dong S, Wang FH, Jin L, Dong J (2020) 3D processing maps of cast Mg-8Gd-3Y alloy at high strain rates and their application in plane strain forging. Int J Adv Manuf Technol 106:133–141
4. Xia XS, Xiao L, Chen Q, Li H, Tan YJ (2018) Hot forging process design, microstructure, and mechanical properties of cast Mg–Zn–Y–Zr magnesium alloy tank cover. Int J Adv Manuf Technol 94: 4199–4208
5. Yuan L, Zhao Z, Shi WC, Xu FC, Shan DB (2015) Isothermal forming of large-size AZ80A magnesium alloy forging with high mechanical properties. Int J Adv Manuf Technol 78:2037–2047
6. Liu B, Zhang ZY, Jin L, Gao JL, Dong J (2016) Forgeability, microstructure and mechanical properties of a free-forged Mg–8Gd–3Y–0.4Zr alloy. Mater Sci Eng A 650:233–239
7. Liu J, Cui ZS (2009) Hot forging process design and parameters determination of magnesium alloy AZ31B spur bevel gear. J Mater Process Technol 209:5871–5880
8. Liu J, Li JQ, Cui ZS, Qu HA, Ruan LQ (2013) Material driven workability simulation by FEM including 3D processing maps for magnesium alloy. Trans Nonferrous Metals Soc China 23:3011–3019
9. Sun CY, Xiang Y, Liu G, Zuo X, Wang MQ, Zhang QD (2017) Extrusion limit diagram of IN 690 super-alloy tube based on hot processing map. Int J Adv Manuf Technol 89:3419–3428
10. Lu J, Song Y, Hua L, Zheng KL, Dai DG (2018) Thermal deformation behavior and processing maps of 7075 aluminum alloy sheet based on isothermal uniaxial tensile tests. J Alloys Compd 767:856–869
11. Li PW, Li HZ, Huang L, Liang XP, Zhu ZX (2017) Characterization of hot deformation behavior of AA2014 forging aluminum alloy using processing map. Trans Nonferrous Metals Soc China 27:1677–1688
12. Sun Y, Feng XY, Hu LX, Zhang H, Zhang HZ (2018) Characterization on hot deformation behavior of Ti-22Al-25Nb alloy using a combination of 3D processing maps and finite element simulation method. J Alloys Compd 753:256–271
13. Du ZH, Jiang SS, Zhang KF (2015) The hot deformation behavior and processing map of Ti–47.5Al–Cr–V alloy. Mater Des 86:464–476
14. Li JQ, Liu J, Cui ZS (2014) Characterization of hot deformation behavior of extruded ZK60 magnesium alloy using 3D processing maps. Mater Des 56:889–897
15. Shang X, Zhou J, Wang X, Luo Y (2015) Optimizing and identifying the process parameters of AZ31 magnesium alloy in hot compression on the base of processing maps. J Alloys Compd 629:155–161
16. Lv BJ, Peng J, Shi DW, Tang AT, Pan FS (2013) Constitutive modeling of dynamic recrystallization kinetics and processing maps of Mg–2.0Zn–0.3Zr alloy based on true stress–strain curves. Mater Sci Eng A 560:727–733
17. Xu C, Pan JP, Nakata T, Qiao XG, Chi YQ, Zheng MY, Kamado S (2017) Hot compression deformation behavior of Mg-9Gd-2.9Y-1.9Zn-0.4Zr-0.2Ca (wt%) alloy. Mater Charact 124:40–49
18. Xu WC, Jin XZ, Shan DB, Chai BX (2017) Study on the effect of solution treatment on hot deformation behavior and workability of Mg-7Gd-5Y-0.6Zn-0.8Zr magnesium alloy. J Alloys Compd 720: 309–323
19. Azimi M, Mirjavadi SS, Salandari-Rabori A (2018) Effect of temperature on microstructural evolution and subsequent enhancement of mechanical properties in a backward extruded magnesium alloy. Int J Adv Manuf Technol 95:3155–3166
20. Chalay-Amoly A, Zarei-Hanzaki A, Changizian P, Fatemi-Varzaneh SM, Maghsoudi MH (2013) An investigation into the microstructure/strain pattern relationship in backward extruded AZ91 magnesium alloy. Mater Des 47:820–827
21. Zhang XY, Mei RB, Li PP, Bao L, Zhang J, Zhou YZ (2016) Numerical analysis of deformation of AZ31 magnesium alloy in

backward extrusion with counter pressure. Mater Sci Forum 861: 216–221
22. Fatemi-Varzaneh SM, Zarei-Hanzaki A, Naderi M, Roostaei AA (2010) Deformation homogeneity in accumulative back extrusion processing of AZ31 magnesium alloy. J Alloys Compd 507:207–214
23. Zeng J, Wang FH, Wei XX, Dong S, Zhang ZY, Dong J (2020) A new constitutive model for thermal deformation of magnesium alloys. Metall Mater Trans A 51A:497–512
24. Ding XF, Zhao FQ, Shuang YH, Ma LF, Chu ZB, Zhao CJ (2020) Characterization of hot deformation behavior of as-extruded AZ31 alloy through kinetic analysis and processing maps. J Mater Process Technol 276:116325
25. Luo J, Li MQ, Yu WX, Li H (2009) Effect of the strain on processing maps of titanium alloys in isothermal compression. Mater Sci Eng A 504:90–98
26. Samantaray D, Mandal S, Bhaduri AK (2011) Characterization of deformation instability in modified 9Cr–1Mo steel during thermo-mechanical processing. Mater Des 32:716–722
27. Murty SVSN, Rao BN (1998) On the development of instability criteria during hotworking withreference to IN 718. Mater Sci Eng A 254:76–82
28. Ma X, Zeng WD, Xu B, Sun Y, Xue C, Han YF (2012) Characterization of the hot deformation behavior of a Ti-22Al-25Nb alloy using processing maps based on the Murty criterion. Intermetallics 20:1–7
29. Güzel A, Jäger A, Parvizian F, Lambers HG, Tekkaya AE, Svendsen B, Maier HJ (2012) A new method for determining dynamic grain structure evolution during hot aluminum extrusion. J Mater Process Technol 212:323–330